Numerical modeling and experimental analysis of air ejectors' transient operation in bleed-air aircraft systems

Eugenio Schillaci[a], Carles Oliet[a,*], Jagadish Babu Vemula[b], Matthieu Duponcheel[b], Yann Bartosiewicz[b], Philippe Planquart[c]

[a] *Heat and Mass Transfer Technological Center (CTTC), Universitat Politècnica de Catalunya – BarcelonaTech (UPC) ESEIAAT, C/ Colom 11, 08222 Terrassa (Barcelona), Spain*

[b] *Université catholique de Louvain (UCLouvain) Institute of Mechanics, Materials, and Civil engineering (iMMC) B-1348, Louvain-la-Neuve, Belgium*

[c] *von Karman Institute for Fluid Dynamics (VKI) EA department Waterloosesteenweg, 72 - B - 1640 Sint-Genesius-Rode, Belgium*

Abstract

The physics and modeling of air ejectors in on- and off-design conditions have been extensively addressed in the past, reaching a good level of maturity. However, to achieve a robust dynamic model at the system scale integrating an ejector, there is a need to develop 0D models suitable for tackling abnormal functioning modes and the transition between them.

The current research focuses on understanding the physical behavior of air ejectors for aeronautical applications. First, the operational envelope with relevant modes and transitions is presented. Hence, an experimental set-up is built to allow direct observation of transient phenomena under typical aeronautical conditions. Complementarily, CFD (RANS and URANS) simulations are employed to gain knowledge of the whole operational envelope, including abnormal modes. Experimental analysis and CFD are employed to show the ejector's quasi-steady behavior under the system's time-scale.

As a final milestone, a 0D model previously implemented is here extended and calibrated using CFD simulations to cover abnormal functioning scenarios as primary closed mode and inverted operation. Finally, some typical

*Corresponding author. Tel.: +34 93 739 81 92; Fax: +34 93 739 89 20.

Email addresses: eugenio.schillaci@upc.edu (Eugenio Schillaci), carles.oliet@upc.edu (Carles Oliet)

transitions belonging to the operational envelope are reproduced and validated compared to experimental data, highlighting the robustness of the implementation.

Keywords: supersonic air ejectors, aeronautical applications, compressible RANS simulations, operational map, 0D model

---

1. Introduction

The implementation of ejectors is getting an increasing interest in many industrial sectors due to its capability of improving the efficiency and reliability of specific thermo-technical systems, especially in the aeronautical and HVAC&R field [1]. In particular, the aircraft sector integrates ejectors for bleed air management, recirculation or ram-air ventilation, and aero-engine cooling [2–4]. In the new generation of aircraft based on Ultra High Bypass Ratio (UHBR) engines, new bleed concepts are analyzed to improve the system's overall efficiency and integration with the wing. An option under analysis consists of employing an ejector that uses the engine bleed air as a primary motive stream to draw and mix a considerable quantity of air from the outside or from a lower-pressure port as a secondary stream. Compared to classic bleed systems, this leads to a reduction in the size of the pre-cooler due to the significantly lower temperature of the air mixture. Moreover, reducing the amount of high-pressure bleed air extracted from the engine leads to a lower power loss for non-propulsive tasks, providing environmental and economic benefits due to the reduction of fuel consumption.

Along with their integration in the systems mentioned, there is a need to correctly model these elements through 0D models (also known as lumped -or reduced models), which allow the prediction and control of the global thermo-technical system in which they are introduced without heavy computational efforts. The modeling of ejectors is a mature practice; however, it was mostly limited to design operation modes, i.e., in the case where the primary flow is supersonic. Several 0D models available in the literature constitute a good and mature basis [5–12]. Many modern ejector models, such as Chen et al. [7], rely on the Fabri-choking theory. According to this theory, the two streams do not mix right away at the exit of the primary nozzle, but they rather conserve their integrity until a particular downstream section, where the secondary stream reaches the speed of sound by passing through an *aerodynamic throat*, i.e., a minimum cross-section as in a Laval nozzle.

More recently, the compound-choking mechanism [13] has been translated into a 0D model by Metsue et al. [9]. The compound choking criterion considers the individual state of each stream from the outlet of the primary nozzle. The compound flow can then be compound-choked, although the Mach number of the secondary stream is less than unity, providing the Mach number of the primary stream is sufficiently supersonic. While most of the identified models work with the primary flow in supersonic conditions, to the best of the authors' knowledge, only a few 0D models perform calculations of convergent ejectors where the primary flow may be found under subsonic conditions, such as Besagni et al. [14], where the Mach number at secondary throat is obtained from CFD simulations, and Zhu et al. [15], where the pressure at the throat is considered equal to the secondary pressure. In our previous work [16], this limitation has been overcome by introducing a modified 0D ejector model capable of working under pure subsonic conditions or considering one closed port (secondary port). The new model can automatically handle different flow conditions, i.e., normal and abnormal modes, employing a conditional structure under the same algorithm. The model was validated and calibrated in static conditions, reproducing stationary working regimes within the operational envelope of applications. However, there is another hurdle before applying the model in dynamic systems: to the best of the authors' knowledge, there are no examples of 0D models used in dynamic process simulation. Only a few examples performed with higher-order numerical models have been provided; however, they still focus on design conditions. Between the others, Van den Berghe et al. [17] developed a 1D unsteady model for supersonic single-phase ejectors, which combines 1D gas dynamics formulations with entrainment and mixing relations. Furthermore, different works employ Computational Fluid Dynamics (CFD) and different kinds of turbulence models to analyze the transition between different conditions [18, 19]. In the current work, it must be proved that our 0D model is capable of correctly simulating the dynamic processes modeling the transition between different operational modes (e.g., Normal Mode to Secondary or Primary Closed Mode).

CFD simulations are equally important for the detailed simulation of ejectors, both at a static level and in transient operation. In particular, RANS (Reynolds-Averaged Navier-Stokes) models are a widely used tool to study ejectors, as reviewed by Besagni et al. [20–22]. RANS is accurate in determining the overall ejector performances to study the effect of geometry [23], can accurately reproduce local flow features [24–26], e.g., shock wave

pattern, and can be used to investigate complex flow phenomena and choking mechanisms [27–30]. In our previous work [16], CFD-RANS simulations were employed to identify and characterize the ejector's global physics and all the possible working modes beyond normal operations, including reverse flow and closed port scenarios. The analysis yielded a map of all the operating regimes encountered in the ejector, which must be considered for the 0D model. Furthermore, the CFD study also provided a deep and comprehensive set of validation tests, which were used to calibrate and verify the newly developed 0D model. Regarding Unsteady RANS (URANS) simulations, those were already used to study the transient behavior of ejectors, especially for the initial transient in vacuum ejectors [18, 31–37], but also for applications in fuel cells [38–40] or to analyze the transient behavior of adjustable needle ejectors [19]. More specifically, [31, 33–36, 39, 40] all used $k-\omega$ based models either $k-\omega$ SST, GEKO or transitional $k-\omega$. In those studies, transient simulations are used to characterize both the global unsteady characteristics of the ejector, i.e., port pressures and mass flow rate, e.g. [39, 40] and the detailed unsteady behavior of the flow within the ejector, e.g. [31, 34, 36]. Higher accuracy models, such as LES, are disregarded due to their computational cost (a few ejector studies are proposed with LES, e.g. [41]), especially because they imply the adoption of 3D domains even for 2D axisymmetric geometries. In the present work, CFD simulations will play a key role in demonstrating the ejector's quasi-staticity in the presented system's time-scale, and a 2D axisymmetric domain is adopted. For this purpose, a URANS model is employed. Furthermore, the static RANS simulations of two modes of operation, i.e. Inverted and Primary Closed Modes, not presented in [16], are used here to validate the application the 0D model in a broader range.

Experimental investigation is also a mature practice to characterize the performance of different ejectors in steady-state conditions for various operating conditions. Transient experimental analysis can also be found in the literature, but mainly for the starting and stopping of the ejectors [42–44]. To the best of the author's knowledge, there are no documented results in the literature regarding transient analysis caused by a significant change in operating conditions that alters the operational mode. Therefore, in the present project, a new test bench was designed and constructed to characterize first different ejector geometries in steady-state conditions with different mass flow and temperature conditions [45–48]. Afterward, the test bench was upgraded to a dynamic test bench to study transient phenomena when

changing from various states, covering all classical operating modes of the ejectors. Unsteady pressure measurements with fast response sensors are used, and a specific technique based on hot wire anemometry, with adequate calibration, has been used to characterize the unsteady mass flows.

The paper is organized as follows. In Sec. 2, the operational envelope of the ejector is introduced, detailing relevant working regimes and transitions. In Sec. 3, the experimental set-up is presented, focusing on its features to perform dynamic measurements. In Sec. 4, the CFD and 0D models are presented. In Sec. 5, an experimental test and CFD simulations are employed to show the quasi-steady characteristics of the ejector in the time-scale of the problem. In Sec. 6, the 0D model is verified and calibrated compared to CFD in the range of conditions relevant for the present work, then, it is validated by comparison to experimental data for the relevant transitions. In Sec. 7, the adaptation of the model to the Modelica environment is explained, together with some robustness tests. Finally, conclusions are drawn in Sec. 8.

Nomenclature

p_0	total pressure
p	static pressure
P	$P = p_0$ if the port is an inlet and $P = p$ if the port is an outlet
T_0	total temperature
T	static temperature
V	velocity
η_p, η_s	isentropic efficiency in primary and secondary
η_m	mixing efficiency
R	$= \frac{p_{0,s}}{p_{0,p}}$ secondary to primary pressure ratio
M	Mach number
ω	$= \frac{\dot{m}_s}{\dot{m}_p}$ entrainment ratio
$\dot{m}_p$	mass flow rate at primary inlet
$\dot{m}_s$	mass flow rate at secondary inlet
$\dot{m}_o$	mass flow rate at outlet
A	$= \pi(\frac{d}{2})^2$ section area

Sub-Indices

p, s, b	primary, secondary, back flow
t	primary nozzle throat
y	end of expansion
m	mixing section
2	diffuser inlet
max	values in choked conditions

2. Ejector behavior: operational envelope, relevant modes and transitions

Ejectors are passive devices with two inlets and one outlet. They enable a low-pressure secondary flow to be entrained and/or compressed by a high-pressure primary flow. The suction required for the entrainment is generated by accelerating the primary flow through a converging-diverging nozzle. The two streams mix in a constant-area zone and the flow is then decelerated in a diffuser to recover pressure from kinetic energy before being discharged at an intermediate back-pressure. A simplified scheme is proposed in Fig. 1.

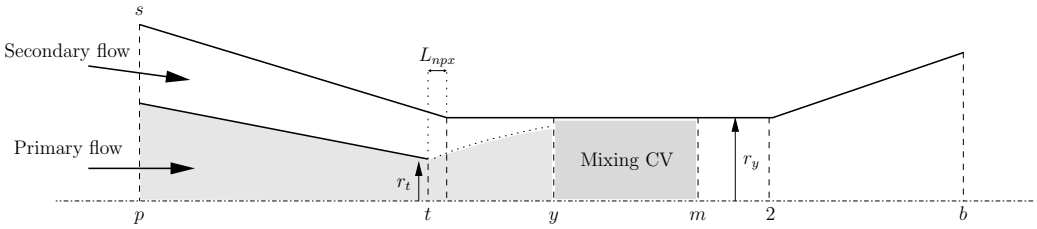


Figure 1: Ejector scheme used to implement the 0D model originally presented in [16].

In the literature, the ejector behavior is typically analyzed using characteristic curves, considered when the primary flow is sonic/choked (design operation). Characteristic curves, see Fig. 2, represent the entrainment ratio, ω, as a function of the back-pressure, p_b. The secondary (induced) flow reaches its maximum flow rate (corresponding to maximum entrainment) in *on-design* conditions where the ejector is double-choked. Conversely, when only the primary flow is choked, the ejector is in *off-design* conditions. However, on the bigger picture, ejector modeling in real systems is not limited to classic design conditions. In the current Section, the global operational envelope of supersonic ejectors, originally presented in Schillaci et al. [16], is summarized. Next, the operating modes relevant to the UHBR engine/bleed-air ejector applications are listed, together with the relevant transition between those modes.

2.1. Operational envelope

The ejector behavior is characterized by the relation expressing the primary and secondary mass flow rates $(\dot{m}_p, \dot{m}_s)$ as a function of port pressures and temperatures $(P_p, P_s, P_b, T_{0,p}, T_{0,s}, T_{0,b})$, thoroughly analyzed in [16]. Those flow rates are positive when the flow enters the domain, while

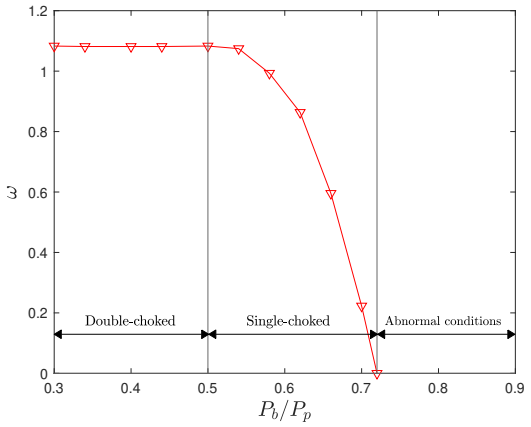


Figure 2: Characteristic curve of an ejector representing entrainment ratio, $\omega = \frac{\dot{m}_s}{\dot{m}_p}$ as function of back-pressure.

the outlet mass flow rate is defined as $\dot{m}_o = \dot{m}_p + \dot{m}_s$, positive when the flow exits the domain. The pressure P at the ports is the total one (p_0) when the flow enters the domain and the static one (p) on the other way. The pressure ratios are the dominant variables in the operational envelope, while the effect of temperature was briefly studied in past works [16, 47]. In the remainder of this section, we will thus investigate the operating map of the ejector in the $(\frac{P_s}{P_p}, \frac{P_b}{P_p})$ plane.

The operating plane is divided according to the sign of the mass flow rates to highlight the different flow regions (Zones 1-6), as reported in Fig. 3. Those regions are delimited by the special cases where one of the three ports is closed: (Limit 1) $\dot{m}_s = 0$, (Limit 2) $\dot{m}_p = 0$ and (Limit 3) $\dot{m}_o = 0$. For those cases, the pressure at the closed port can be obtained from the simulations. The case with $\dot{m}_s = 0$ is also known as the *vacuum* ejector, where the ejector sustains a vacuum at the secondary port without mass flow rate. In the *started* mode, the maximum expansion of the primary jet at the entry of the mixing duct is faced, yielding the lowest secondary pressure. In this mode, the secondary pressure is not sensitive to the back-pressure. This corresponds to the horizontal part of the $\dot{m}_s = 0$ line. In the *unstarted* mode, the primary jet reattaches further downstream inside the mixing duct. The secondary pressure is then sensitive to the back-pressure. This corresponds to the increasing part of the $\dot{m}_s = 0$ line. The part of the $\dot{m}_s = 0$ line where $\frac{P_b}{P_p} > 1$ corresponds to the reversed flow conditions where the fluid flows from the outlet to the primary port.

In the $\dot{m}_p = 0$ case, when $P_s > P_b$, the flow enters via the secondary inlet and creates a lower pressure in the primary nozzle. Note that this low pressure is vacuum only in the upper right quadrant where $\frac{P_b}{P_p} > 1$, whereas, in the upper left quadrant, we obtain $P_b \leq P_p \leq P_s$. Similarly to the $\dot{m}_s = 0$ case, started and unstarted regions can also be observed.

The region where both primary and secondary flow rates are positive, i.e., the normal operation of the ejector, lies between the $\dot{m}_s = 0$ and $\dot{m}_p = 0$ lines on the left of the map. In cases with $\frac{P_s}{P_p} < 1$ and above Limit 1, the ejector is in normal operation (Zone 1a), including design and abnormal conditions [16]. For $\frac{P_s}{P_p} > 1$ and left/bottom of Limit 2, the ejector behaves as a mixing device where both primary and secondary pressures are higher than the back-pressure (Zone 1b).

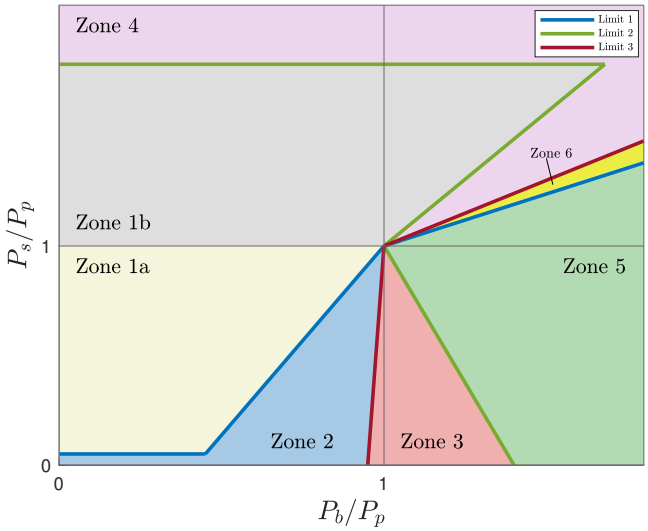
All the remaining parts of the operating plane correspond to cases with at least one port with reversed flow conditions: reverse flow at the secondary port (Zone 2); flow reversal occurs at the outlet port (Zone 3); equivalent of Zone 2, but when the driving flow enters from the secondary port: $\dot{m}_s > 0$, $\dot{m}_p < 0$ and $\dot{m}_o > 0$ (Zone 4); fully reversed state where the flow enters the outlet and exits from both primary and secondary ports (Zone 5); flow enters from the secondary and back and exits from the primary (Zone 6, narrow region).

A particular operational envelope for a specific ejector geometry can be obtained using CFD simulations, as proposed in [16]. This operational envelope is employed in the present work and reported in Fig. 7.

2.2. Relevant operating conditions

In the UHBR engine bleed-air systems, the ejector is connected to the primary –high-pressure (HP) port and secondary –intermediate-pressure (IP) ports of the compressor. The ejector's main role is to provide proper inlet conditions to the downstream aircraft pneumatic systems, e.g., pre-cooler, by adjusting the pressure at the two inlet ports by means of valves. Referring to the previous section, the ejector mostly operates in Zone 1 but also with closed primary or secondary ports (Limit 1 and 2). Some limited reversed flows can also occur and may be considered in complex transient operations of certain specific systems (e.g., failure modes); however, continuous operation deep inside the reversed flow regions is of lesser practical relevance for the current application. Summarizing, the covered modes are the following:

1. **Zone 1a (Normal Mode)**: corresponding to the normal operating



Limit 1: $\dot{m}_s = 0$
Limit 2: $\dot{m}_p = 0$
Limit 3: $\dot{m}_o = 0$
Zone 1a: $\dot{m}_p, \dot{m}_s, \dot{m}_o > 0$, $\frac{P_s}{P_p} < 1$
Zone 1b: $\dot{m}_p, \dot{m}_s, \dot{m}_o > 0$, $\frac{P_s}{P_p} > 1$
Zone 2: $\dot{m}_p, \dot{m}_o > 0$, $\dot{m}_s < 0$
Zone 3: $\dot{m}_p > 0$, $\dot{m}_s, \dot{m}_o < 0$
Zone 4: $\dot{m}_p < 0$, $\dot{m}_s, \dot{m}_o > 0$
Zone 5: $\dot{m}_o, \dot{m}_s, \dot{m}_o < 0$
Zone 6: $\dot{m}_p, \dot{m}_o < 0$, $\dot{m}_s > 0$

Figure 3: Operating plane of the ejector with the zones delimited by the limit cases for fixed temperature ratios $\frac{T_{0,s}}{T_{0,p}} = \frac{T_{0,b}}{T_{0,p}} = 1$.

mode, pressure provided at primary and secondary ports (HP+IP), with $p_{p0} > p_{s0}$. Primary and secondary flows are positive and can be in super –or subsonic– conditions. No reverse flows.

2. **Zone 1b (Inverted Mode)**: primary and secondary flows are positive (HP+IP) and can be in super –or subsonic– conditions. $p_{s0} > p_{p0}$, consequently, the secondary flow provides an entrainment effect over the primary. This condition only happens during transitions.
3. **Limit 1 (Secondary Closed Mode)**: the secondary port is kept closed while the primary flow is positive (only HP). It occurs when the primary pressure is sufficient to provide proper downstream conditions.
4. **Limit 2 (Primary Closed Mode)**: the primary port is kept closed, and the secondary flow is positive (only IP). Occurs when the system pressure is provided by the secondary port.
5. **Zones 2-6 and Limit 3 (Reverse flows modes)**: reverse flow through primary and secondary ports. Only occur during transitions between modes.

In the present work, the working modes related to **operational regimes** are analyzed, i.e., those occurring during flight operation. Consequently, the validation and analysis focus on Items 1-4 of the above list and comprises the main transitions between them, listed in the next sub-section. Reverse

flows (Item 5) are briefly treated in Sec. 7 in the context of model robustness in system software.

2.3. Relevant transitions

The two main transitions analyzed experimentally and numerically in the present work are reported within the operational map in Fig. 4. Transition 1 consists in the passage from Zone 1a (HP+IP) to Limit 1 (only HP), while Transition 2 goes from Zone 1a (HP+IP) to Limit 2 (only IP). Details are given below.

2.3.1. Transition 1

The ejector transitions from the normal operating mode (Zone 1a) to the Secondary Closed Mode (Limit 1), as depicted in Fig. 4, or vice-versa. This transition can occur in the following flight situations: (a) the ejector initially operates with both ports open (HP+IP) and produces an entrainment effect. However, due to changes in flight conditions and/or working conditions of the compressor, the inlet pressures may be reduced to unacceptable levels, causing an excessive reduction of the mass flow and/or pressure provided at the ejector outlet or a flow temperature outside of an acceptable range. Hence, the secondary valve closing is triggered, and the ejector rapidly starts to operate with HP only, providing the necessary mass flow/pressure/temperature at the outlet port. (b) As normal working conditions are re-established, the secondary valve can be reopened, thus recovering efficient operating conditions due to less bleeding from the HP port.

In Sec. 6.2.1, the transition between the Normal Mode and the Secondary Closed Mode is studied experimentally, driven by the opening and closing of the secondary valve. The same situation is reproduced by the numerical method to validate its accuracy during its dynamic transition. The transition placed in the operational map does not imply any reverse flow, and it is already covered by regimes already validated in [16], i.e., Normal mode and Secondary Closed case.

2.3.2. Transition 2

The ejector transitions from the normal operating mode (Zone 1a) to the primary closed mode (Limit 2), as depicted in Fig. 4 or vice-versa. The transition occurs when: (a) the downstream pressure can be provided by the secondary port only (only IP), hence, the primary port can be closed, leading to energy savings. (b) Vice versa, when the IP pressure alone is insufficient,

the primary (HP) port is opened to activate the entrainment. The predicted path in the operational map indicates a potential crossing of the top-left and/or top-right quadrant (Zone 1b). Zone 1b and Limit 2 were uncovered by the static analysis presented in [16]. Hence, in Sec. 6.1, the capability of the 0D model to reproduce the ejector in those zones (with steady-state operation) is simulated and validated by comparison to CFD simulations. In Sec. 6.2.2, the mentioned transition between Normal Mode and Primary Closed Mode is studied experimentally, driven by the opening and closing of the primary valve, and then reproduced by the numerical method to validate its accuracy during its dynamic transition. Moreover, in Sec. 5.2.3, Transition 2 is studied numerically, driven by the variation of the primary mass flow, to validate the quasi-steady assumption and accurately measure the system response time-scale in the context of a closing port.

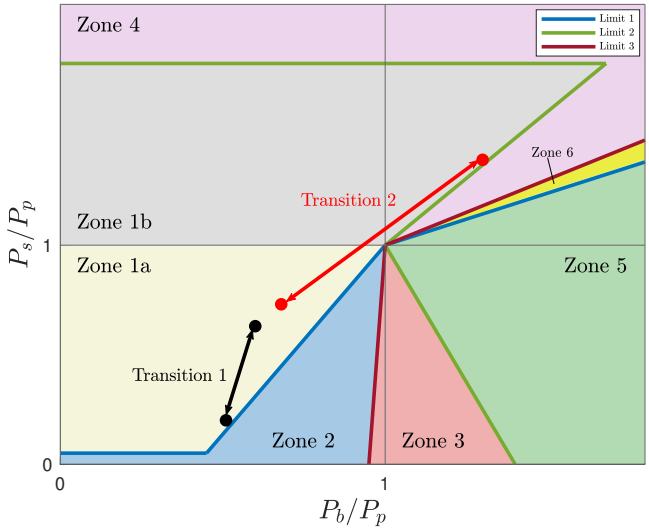


Figure 4: Relevant transitions within the operational map.

3. Experimental Set-up

The experimental test bench employed in the current paper was already employed in past works [45–48] to obtain detailed insights into a set of ejectors for aeronautical applications. Moreover, the work included the manufacturing of a set of original ejector prototypes [45].

The experimental test bench was built in two phases. The first one was focused on obtaining static experiments under different operating modes. The system is fed with compressed air at ambient temperature. The flow is then split into two separate pipes (primary and secondary lines). Pressure regulators allow pressure regulation from 1 bar to 8 bars within each line. After the pressure regulators, a control valve is installed to adjust the flow rate within each line. The flow is then directed through two flexible stainless steel tubes to the entrance of primary or secondary ejector ports. These flexible tubes allow the option of supplying heated air to either line, depending on the test matrix, by deviating one of the flows through the electric heater (maximum heating power of 150 kW). Finally, a pressure regulation valve at the outlet of the final vertical straight tube enables control of the back-pressure. The mass flow of each line is measured with Kobold vortex mass flow meter (accuracy of 1% for the volumetric flow rate and 1.5% for the mass flow rate). Validyne pressure sensors (1% error band) have been used to measure steady-state pressure, while flush-mounted Kulite pressure sensors (0.5% error band), which have a response time of 0.0001 s, have been used to characterize fast pressure changes during transient operations.

The test campaign has been extensive in the static regime, consolidating the understanding of the ejector physics and behavior under normal and abnormal conditions. Some results were presented in [45, 48], where operating conditions belonging to Zone 1a and Limit 1 were tested to allow the validation of the 0D model. The effect of flow heating using the electric heater was tested in [47].

The second and definitive test bench, described in Fig. 5, consisted of an adaptation of the initial one to allow the analysis of ejector transitions. The pressure regulators connected to the compressor in the initial set-up have a response time of 5 s when opening and 2 s when closing. These response times are too lengthy to effectively control transients, so fast-response three-way valves have been installed. Additionally, a three-way valve is necessary to redirect the flow, particularly when reproducing an inlet opening or closing scenario. This set-up allows the main flow to bypass through a side branch, preventing unwanted behavior from the pressure regulators. Fast response three-way valves at the inlet ports and a fast valve at the outlet allow for the covering of transitions, providing an opening/closing time of 1000 ms, which is representative of the time-scale of the system.

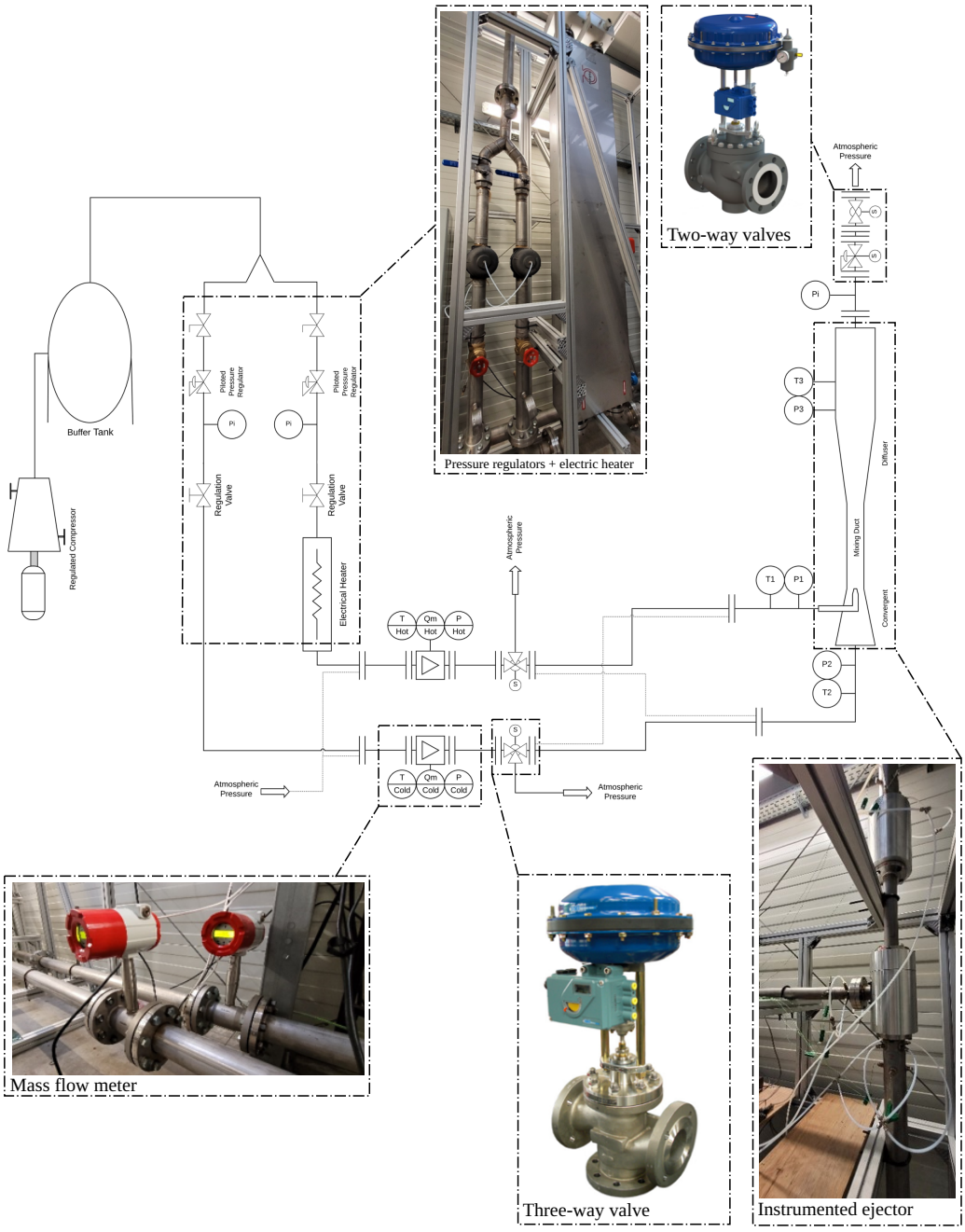


Figure 5: Sketch of the test bench for ejector dynamic analysis. Highlight the main elements of the set-up.

Fast-response pressure transducers have been installed at each port to follow the pressure evolution (Validyne pressure transducers or Kulite pressure sensors). A hot wire sensor was added to the baseline vortex flowmeters to identify an adequate time response to the velocity changes, given that the flowmeter response is not sufficiently fast to capture flow variation in the time-scale of the system, i.e., when the valve is closed at primary or secondary port. The hot wire sensor has been calibrated under static conditions against the flowmeter to obtain a fair estimation of the flow rate within the transients. The electric heater can be connected to one of the two lines to heat up primary or secondary flow. However, no results considering the heating effect have been reported in the present work. Preliminary results obtained in transient operations are reported in [46].

In the context of the present work, the main operative transitions between the static regimes have been experimentally characterized, i.e., Transition 1 and 2. The results have been employed to validate the 0D model in the mentioned scenarios. Only one of the manufactured ejector prototypes was tested in the present work. Its shape and dimensions coincide with the ones presented in Fig. 6 and are employed for CFD simulations.

4. Numerical models

4.1. CFD model

CFD simulations are used to perform steady-state and transient simulations of ejectors. The commercial CFD package Ansys Fluent (version 2020 R2) is utilized to model the flow within the ejector, with a structured mesh generated by the Ansys meshing tool. The domain consists of the ejector geometry employed for experimental analysis, whose section is reported in Fig. 6. The investigated ejector geometry is essentially axisymmetric, with the bend in the primary nozzle pipe being the only 3D feature of the geometry (Fig. 6). The geometry was simplified to perform the simulations in a 2D-axisymmetric domain extracted from the 3D geometry as shown in Fig. 6. The computational domain is based on the shaded region, and some extensions were added to ensure proper outflow conditions. The primary nozzle is convergent only, providing a sonic jet at the exhaust when operating under normal conditions. The ejector geometry is proprietary, and the dimensions cannot be detailed; however, parameterized information on the main sizes, indicated in Fig. 6, is given in Tab. 1. The mesh includes approximately 641485 quadrilateral elements, determined from the mesh convergence study

reported in [16]. The grid is refined in the near-wall regions to capture the boundary layers with $y^+ < 1.55$ and in the region between the primary nozzle exit and entry of the mixing chamber to capture the pseudo shock train.

In static RANS simulations, the $k-\omega$ SST turbulence model is used as it was shown in the literature and in preliminary simulations to give the most accurate results for global and local quantities [20, 21, 27, 49]. Steady-state flow convergence is achieved using the coupled solver with an ideal gas law assumption. Boundary conditions include total pressure at the inlets of the primary and secondary nozzles and static pressure at the ejector outlet. For simulations with closed valves, inlet/outlet sections are replaced by a wall boundary condition at the corresponding port. No-slip and adiabatic boundary conditions are applied to surfaces. Detailed validation and verification studies are reported in [16, 45]. In URANS simulations, the time-dependent flow convergence is achieved by using the Pressure-Implicit with Splitting of Operators (PISO) solver with CFL 0.8. The total number of time steps in the transient simulation depends on the timesteps and total timespan. Regarding the boundary condition types, a variable stagnation pressure condition (pressure inlet) or variable mass flow rate (mass flow inlet) is imposed at the primary inlet, and secondary inlet and outlet sections are at constant pressure and vice-versa.

CFD simulations are used for several purposes: (1) to obtain the operational envelope by marking the different modes of operation (i.e. the operational envelope of Fig. 3 for a specific ejector geometry) using steady-state simulations and (2) to verify the quasi-static operation of the ejector by performing transient simulations, reported in Sec. 5. The first objective was basically achieved in [16] by performing the simulations marked in Fig. 7. Part of the data, i.e., those related to Zone 1b and Limit 2, are employed in the present work to validate and calibrate the 0D model in the specific zones needed to employ the ejector model in transient scenarios.

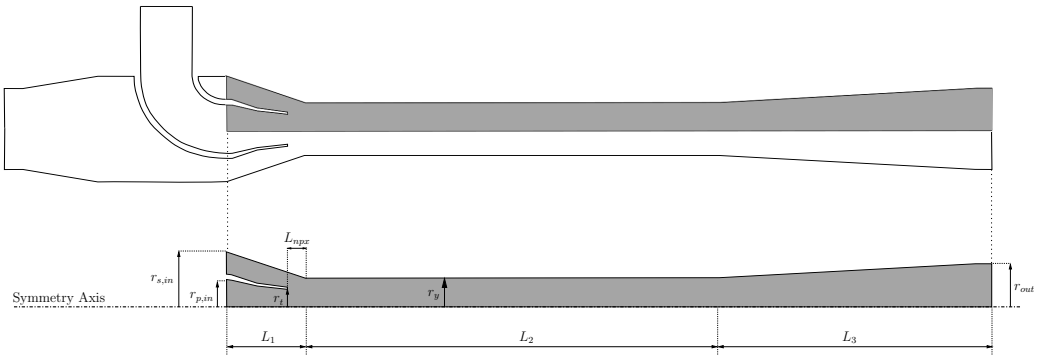


Figure 6: Top: cross-section of the 3-D geometry of the ejector highlighting the axisymmetricity. Bottom: 2-D axisymmetric region employed in CFD simulation.

r_t/r_y	L_{npx}/r_y	$r_{p,in}/r_y$	$r_{s,in}/r_y$	r_{out}/r_y	L_1/r_y	L_2/r_y	L_3/r_y
0.56	0.56	0.91	1.70	1.52	2.42	14.44	8.88

Table 1: Dimensionless sizes of the ejector studied in the current paper.

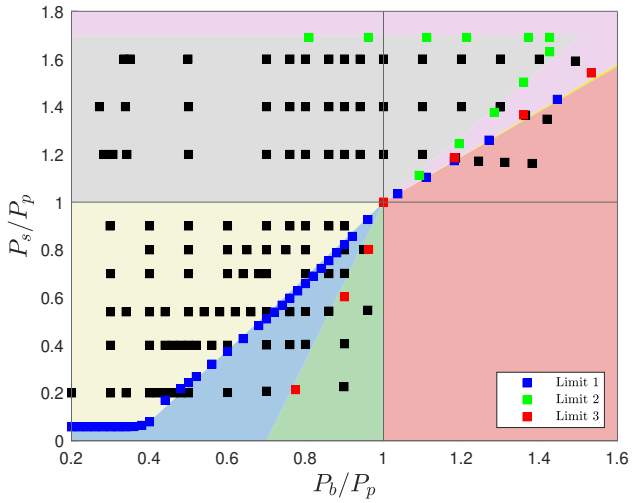


Figure 7: Operating plane of the ejector analyzed in the present work. Square points indicate the static numerical simulations performed, while the colored areas reflect Zones 1-6 introduced in Sec. 2.

4.2. 0D model

The 0D ejector model employed in this work is designed to extend the operational perimeter of previous methods like Chen et al. [7] or Metsue et al. [9] to working conditions that are not strictly on- or off-design (choked primary flow). The objective is to cover the functioning of the ejector in the whole operational perimeter introduced in Sec. 2.2. The model is originally presented in Schillaci et al. [16], where a detailed description of the methods and the resolution algorithms is proposed. For the purpose of clarity, the ejector scheme is depicted in Fig. 1, indicating all the sections involved for the calculation of internal variables. The model is automatically able to handle different flow conditions, i.e., double-choked, single-choked, and unchoked/subsonic flow, with the primary flow provided on both ejector ports. Moreover, the model is capable of dealing with abnormal conditions, such as Primary and Secondary Closed port modes, thanks to its conditional structure under the same iteration cycle. The gas is represented by means of ideal gas properties. In the original work [16], the validation and calibration focus on the capability of dealing with steady situations in which the ejector works in supersonic –with choked or unchoked secondary flow– and subsonic conditions, or in abnormal situations, such as in Secondary Closed regime.

Previously, the model was validated compared to experimental results obtained in static conditions [45, 47]. This allowed the validation of the model in a part of the operational envelope limited to *design* working conditions (double-choked, single-choked) and bounded by the possibilities of the experimental set-up in terms of pressure and temperature ratios. In particular, in [45], the Normal Mode of operation was validated experimentally for two different values of R, together with an abnormal mode (Secondary Closed regime) for two different pressure values. In [47], the thermal effect was tested and compared to experimental values, assessing the effect of increasing the primary flow temperature. Those tests, although useful for validating the model in a part of its on- and off-design modes of operation, are not representative of the entire operational envelope; consequently, the more extended CFD results introduced in [16] were used to validate the 0D model over the whole operational envelope relevant for steady-state operations.

In the present work, the validation of the model focuses on the regimes that are relevant in transition scenarios, i.e., the Inverted Mode (passage through Zone 1b) and the Primary Closed mode (Limit 2). As a hypothesis, when $\frac{P_s}{P_p} > 1$, the ejector considers the secondary flow as the primary while

the primary flow is the entrained one. The maximum secondary flow is calibrated by correcting the throat area, considering $A_{ts} = (A_y - A_t)C_s$, where C_s is the coefficient that best fits CFD data. The complete numerical procedure is explained in [16], and a simplified scheme is reported in Algorithm 1.

Algorithm 1 Main algorithm for the calculation of $\dot{m}_p$ and $\dot{m}_s$.

Check $\frac{P_s}{P_p}$ and set normal or inverted P_p and P_s
Eval. $\dot{m}_{p,\max}$ by flow maximization
Eval. $\dot{m}_{s,\max}$ and $p_{\max,\text{comp}}$ by flow maximization
Guess p_y
while $p_b^* \geq p_b$ **and** $p_y \geq p_{\max,\text{comp}}$ **do**
    if $\dot{m}_p < \dot{m}_{p,\max}$ **then**
        Eval. subsonic primary flow $\dot{m}_{p,\max}$
    else
        Set supersonic primary flow $\dot{m}_p = \dot{m}_{p,\max}$
    Eval. primary flow throat A_{py}
    if $\dot{m}_s < \dot{m}_{s,\max}$ **then**
        Eval. subsonic secondary flow $\dot{m}_{s,\max}$
    else
        Set supersonic secondary flow $\dot{m}_s = \dot{m}_{s,\max}$
    Eval. mixing section properties $p_m, V_m, T_m, \rho_m, M_m$
    if $M_m < 1.0$ **then**
        $p_2 = p_m$, $M_2 = M_m$
    else
        Eval. p_2, M_2 after shock
    Eval. p_b^* at diffuser outlet
    $p_y = p_y - \Delta p$

5. Validation of the quasi-steady assumption

The experimental analysis and the CFD model were employed to verify the quasi-static behavior of the ejector in the time-scale of the system, defined by the characteristic closing time of the valves (around 1000 ms). The behavior of the ejector can be assumed quasi-steady if the time-scale of the intrinsic transient response of the ejector itself is much smaller than the time-scale of the global system. For this reason, static results (obtained at fixed $\frac{P_b}{P_p}$ and $\frac{P_s}{P_p}$) have been compared with those obtained in transient conditions. First, the quasi-steady behavior was checked by means of an experimental

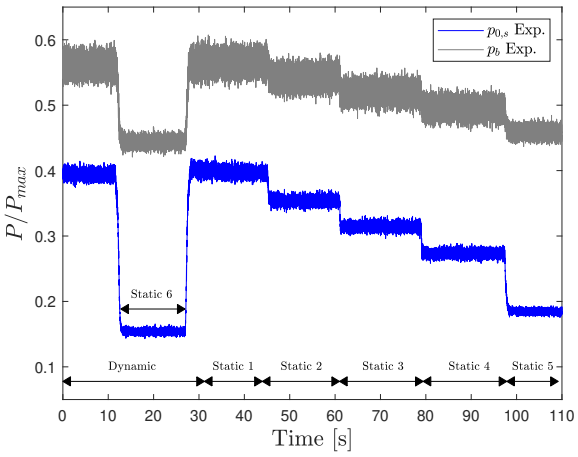
test reproducing Transition 1. Next, CFD simulations helped to understand the characteristic time-scale of the ejector with more accuracy and analyzed different opening/closing scenarios.

5.1. Experimental test

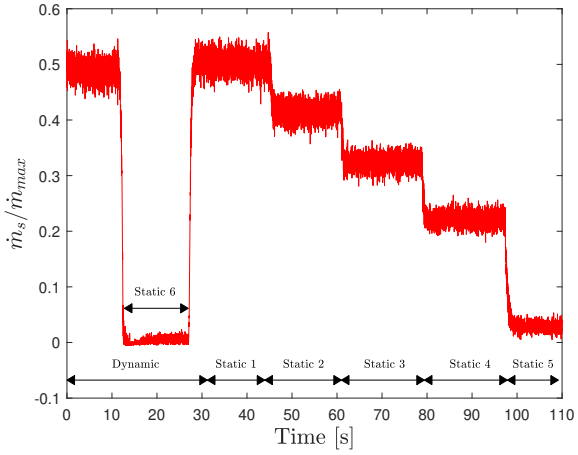
In this test, a transient experiment is performed, and the results obtained are compared with those of six different static tests to verify the quasi-steady behavior of the ejector. The typical time-scale for the three-way valve to open or close is 1000 ms. The flow field inside the ejector, however, reacts more quickly, suggesting that the different transients can be considered to follow a quasi-steady approach.

In Fig. 8, the dynamic test is presented, consisting of the closing and opening of the secondary valve, followed by a sequence of six static tests. These six static tests correspond to different configurations, ranging from the secondary valve being fully open (static 1) to fully closed (static 6 – included within the dynamic segment), with static 2 through static 5 representing partial closures of the secondary valve. Pressure signals are depicted in Fig. 8a. Primary pressure is not reported as it remains stable ($p_{0,p}/p_{max} = 1$), while pressure at the back port drops as the secondary valve closes. The mass flow signal for the secondary flow (Fig. 8b) provided by the hot wire indicates that the flow's response time is around 1000 ms when the valve closes completely during the dynamic part, which aligns with the closing time of the three-way valve, as depicted in Fig. 8c that reports both pressure and mass flow details in the dynamic opening segment of the plot. Primary mass flow is not reported as it keeps stable at 1.

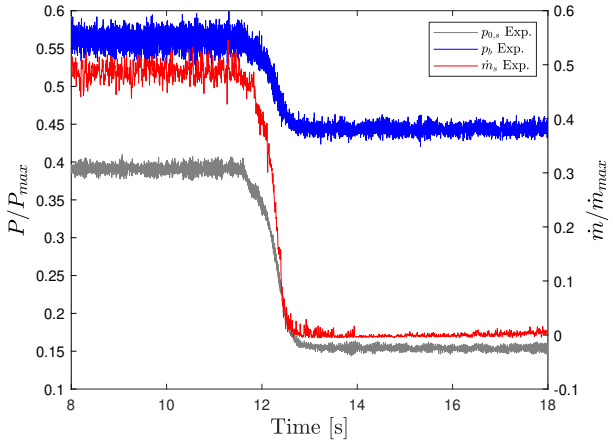
Fig. 9 provides a more detailed analysis of secondary pressure and secondary mass flow obtained in the dynamic part of the test, compared with the data from the six static tests added to the graph. Data are plotted as a function of p_b to allow a direct comparison between dynamic and static cases. In those figures, the continuous curves represent a zoomed-in view of the pressure and mass flow changes during the closing of the secondary valve, while the different points correspond to the operating conditions of the six static tests. During the transient test, it is clearly observed that, despite the inherent noise due to the turbulent nature of the process, the ejector behavior aligns with the different static states, indicating that the transient behavior can be considered a successive series of static configurations, thereby confirming that a quasi-steady approach can be applied to analyze the different transients.



(a) Pressure signals

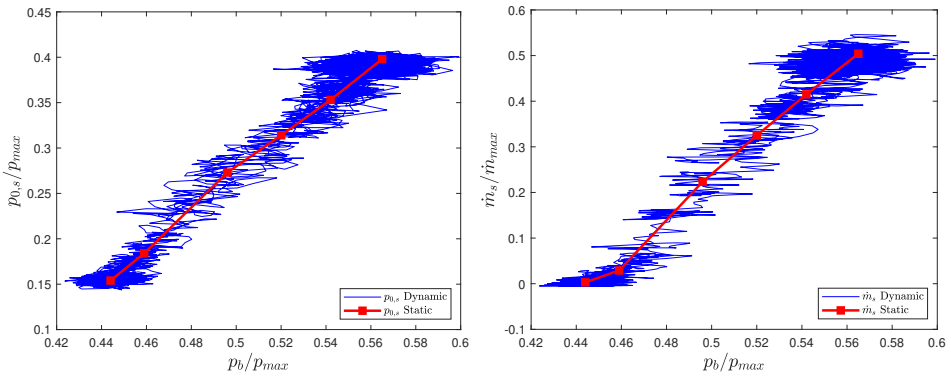


(b) Mass flow signal



(c) Signals during dynamic opening

Figure 8: Sequence of dynamic and static tests performed with the experimental set-up.



(a) Pressure (b) Mass flow

Figure 9: Comparison between dynamic and static signals.

5.2. Numerical tests

Once experimental tests confirmed the quasi-steady behavior, CFD simulations widened the analysis by studying different kinds of transient situations (not reproducible by the experimental set-up) where pressure profiles at the ports are directly imposed as boundary conditions, i.e., abrupt or linear increment of primary pressure.

5.2.1. Abrupt increment of primary pressure

In a first test, the inlet pressure, $p_{0,p}$, is changed abruptly from from $p_{0,p}/p_{0,p,\max}$=0.3 to $p_{0,p}/p_{0,p,\max}$=0.5, keeping all other boundary conditions unaltered. Fig. 10 plots the evolution of the mass flow rates against the flow-time. The transition is triggered after 5 ms. The dashed lines in the plots are the values of the respective parameters computed from the converged steady-state solver solution for the final pressure conditions. These unsteady parameters approach the steady-state solver results as the flow marches with time. Therefore, the flow field achieves the temporally stable solution roughly after 20 ms for this transition scenario. This timescale thus corresponds to the response time of the ejector to a modification of the primary pressure.

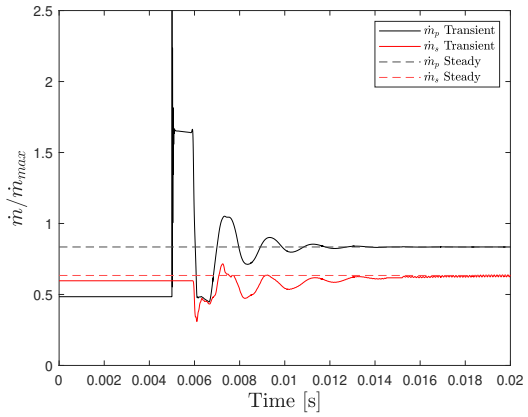
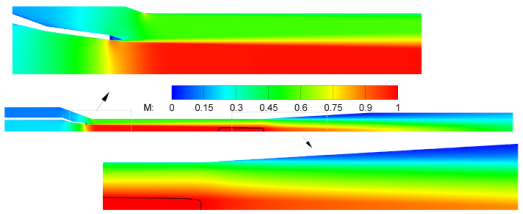
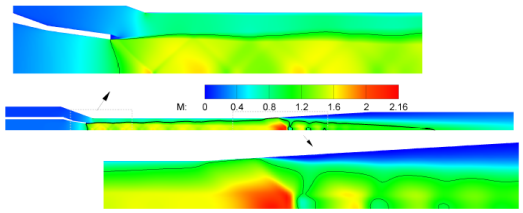


Figure 10: Evolution of the mass flow rates against the flowtime. Pressure at the primary inlet is increased suddenly from $p_{0,p}/p_{0,p,\max}$=0.3 to $p_{0,p}/p_{0,p,\max}$=0.5.

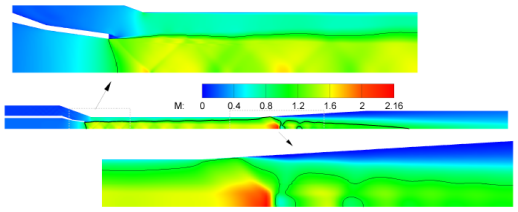
Mach number maps at the initial and final states are shown in Fig. 11. In the initial state, Fig. 11a, the primary flow does not attain the choked condition at the throat, leading to a limited expansion of the primary stream after the throat. Thus, the secondary flow expands as the static pressure decreases at the exit of the primary nozzle, and the secondary mass flow rate is larger than the primary one. As the flow accelerates inside the mixing chamber, a region corresponding to the sonic regime is observed at the end of the mixing chamber. In the final state, Fig. 11b, the flow expands inside the mixing chamber to supersonic velocities through a shock train. As the primary nozzle stream expands downstream, its velocity increases, and static pressure decreases relatively lower than the secondary flow stagnation pressure. As a result, the secondary flow accelerates towards the low static pressure region. During this process, the primary flow goes through a series of oblique shock waves interacting with the shear layer. Fig. 11c shows the Mach number after the transient evolution in URANS simulations, highlighting it matches steady-state Mach contours.



(a) Initial state at $p_{0,p}/p_{0,p,\max}$=0.3



(b) Steady-state simulation at $p_{0,p}/p_{0,p,\max}$=0.5



(c) Transient simulation at $p_{0,p}/p_{0,p,\max}$=0.5 (final time)

Figure 11: Mach contours obtained from the steady-state and unsteady simulations.

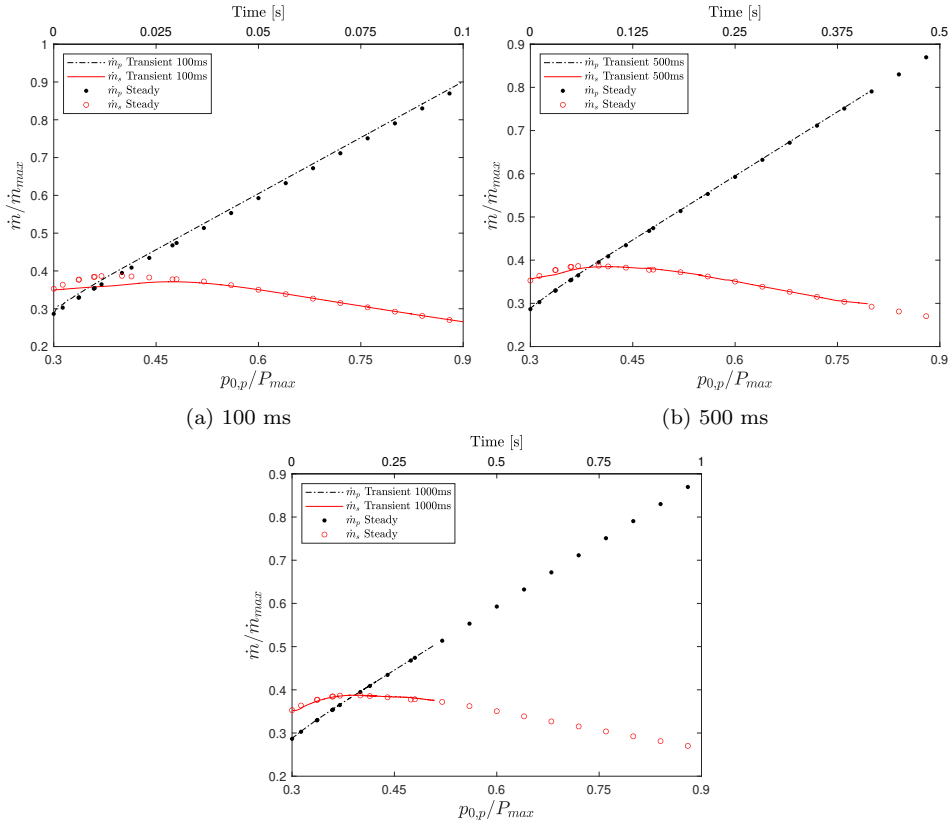
5.2.2. Linear increment of primary pressure

In this case, the transient characteristics of the ejector are investigated with a linear increment of pressure at the primary inlet from $p_{0,p}/p_{0,p,max} =$ 0.3 to 0.9 for three different time spans: 100, 500, and 1000 ms. This consists of the transition between two normal operating points. In particular, the primary nozzle pressure is linearly varied from low to high. In contrast, the secondary inlet and outlet boundaries are at ambient conditions. To verify the quasi-steady assumption, the mass flow rate histories measured at the boundaries in the unsteady simulations are compared with the steady-state solver simulation results.

As reported in Fig. 12a in the case of 100 ms time-span, the mass flow rates computed from the unsteady simulation differ from the steady-state results during the early transient. The primary and secondary mass flow rates show a trend of increment and decrement within 25 ms. The maximum

deviation in the primary mass flow rate is about 10 percent, relatively higher than steady-state solver results. After, the mass flow rate gets stable and shows higher values than the steady state solver solutions with a 5% offset. Conversely, the secondary mass flow rate and entrainment ratio approach the steady state solver solution after 30 ms, while notable differences are highlighted in the first simulation instants.

On the other side, the flow characteristics obtained from the simulations with 500 and 1000 ms time-spans are very close to the steady-state solver results, even during the initial phases, as shown in Figs. 12b and 12c. Simulations for time spans of 500 and 1000 ms are not performed for the whole time range due to the heavy computational cost and only for the time needed to show the convergence to the steady-state solution. Therefore, the ejector behavior is already almost quasi-steady for a time span of 100 ms, and the quasi-steady assumption is very accurate for transitions between two normal operating points with a time span of 500 ms or more. A direct comparison of the different solutions, as a function of the inlet pressure, is reported in Fig. 13, showing the solution convergence as the time span increases.

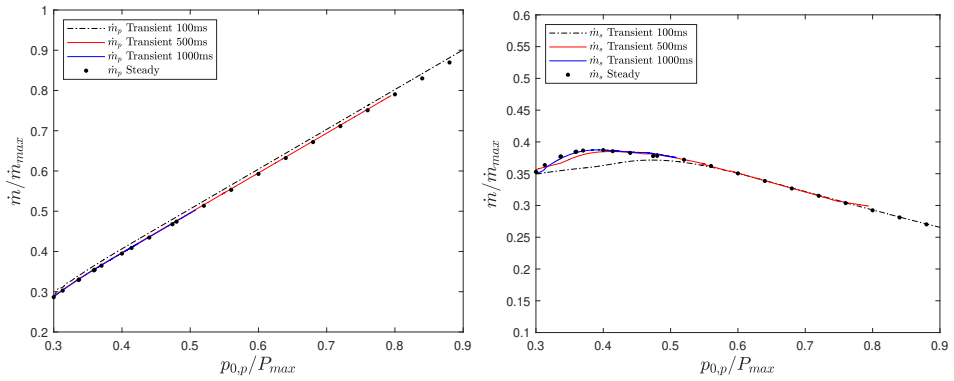


(a) 100 ms

(b) 500 ms

(c) 1000 ms

Figure 12: Time evolution of the mass flow rates for the inlet pressure variation over different time spans. Primary inlet total pressure varies linearly from $p_{0,p}/p_{0,p,max} = 0.3$ to 0.9.

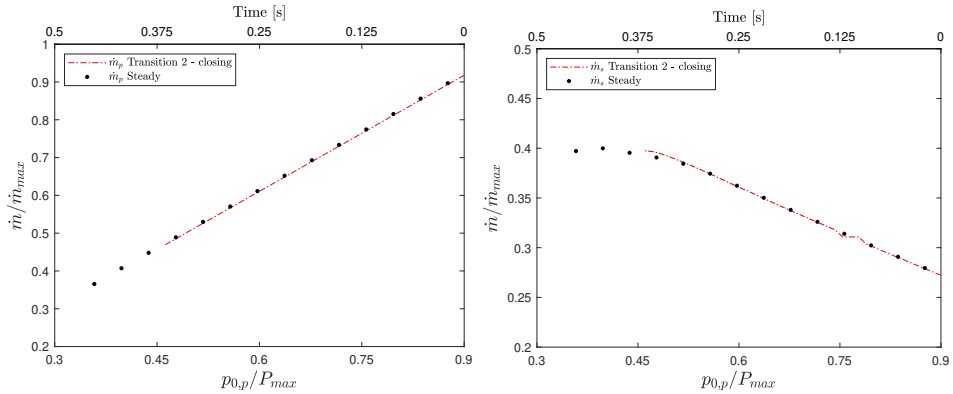


(a) (b)

Figure 13: Mass flow rates as a function of inlet pressure obtained for different time spans in transient simulations, and comparison to steady-state simulations.

5.2.3. Closing primary port

The mass flow rate at the primary inlet is varied linearly for the present transient simulation while the secondary total pressure is kept constant. This case mimics Transition 2, as it represents the closing of the primary port by decreasing $\dot{m}_p$. The mass flow rate at the primary inlet is given as a linear function of flow time, and the time-span of the ramp is 500 ms. In contrast, the secondary inlet and outlet boundaries are at ambient conditions. Fig. 14 presents the evolution of the mass flow rates and primary total pressure against the primary mass flow rate. Time evolution, going from right to left, is shown on the top x-axis. Also in this case, the transient results match well with steady-state solver results, confirming that the time span of 500 ms is acceptable for the flow to be quasi-static.



(a) (b)

Figure 14: Evolution of the mass flow rates and inlet pressure with the primary mass flow rate. Primary mass flow rate is varied linearly in time from max to zero and vice-versa within 500 ms.

6. Validation of the 0D model in transient operation

6.1. Calibration in the Inverted and Primary Closed Modes by comparison to CFD

To accurately simulate the transition processes, the 0D model must be capable of reproducing the ejector behavior in Zone 1b (Inverted Mode). The 0D model is run under those conditions and calibrated compared to CFD data obtained with $\frac{P_s}{P_p} > 1$. The classic characteristic curves of the ejector are obtained by keeping a constant secondary to primary flow pressure ratio while varying the back-pressure. Curves at three different values of R are obtained to compare with the CFD results. In particular, the following values for R are tested: 1.2, 1.4, and 1.6.

The analysis of CFD data allows us to obtain relevant insights regarding the choking mechanism and flow behavior within the mixing zone of the ejector. In particular, as shown in Fig. 15, the throat area for the secondary flow expansion, which here acts as the primary flow, keeps approximately constant as R increases located in the space between the secondary converging duct and the primary nozzle. Consequently, we use the hypothesis that in the Inverted Mode, the ejector works according to the 0D ejector model already presented but with the ports inverted.

Results in terms of $\dot{m}_p$ and $\dot{m}_s$ are reported in Fig. 16, together with the reference CFD data. The plots collect results obtained with the Inverted

Mode and those obtained for $\frac{P_s}{P_p} < 1$, already introduced in [16]. In the Inverted Mode, $\dot{m}_s$ acts as the primary flow. Its prediction is good for R> 1, as shown in Fig. 16b, where only slightly over-prediction is observed for R= 1.6. The flow shows subsonic behavior in all three characteristic curves and for $\frac{P_b}{P_p} > 1$. It is especially visible for R=1.2 and 1.4. The entrained flow is $\dot{m}_p$, reported in Fig. 16a. Despite some offset for R=1.2 and 1.4, the prediction is reasonably good and catches the decreasing part of the curves.

Fig. 17 shows mass flow prediction in situations where the secondary port (Limit 1) or the primary port (Limit 2) are closed. CFD simulations consider this by employing a wall boundary condition at the closed port. The 0D simulations are performed by using the pressure obtained in CFD at the closed port $p_{s0,\mathrm{CFD}}$ or $p_{p0,\mathrm{CFD}}$ as a boundary condition and then verifying that the secondary or primary mass flow rate are essentially zero. The Limit 1 case was already presented in [16] with higher detail. In those cases, the internal pressure p_y evaluated by the model naturally equals the pressure at the closed port set as boundary conditions. This places the working conditions of the ejector exactly on the line marked as Limits 1 and 2 on the operational map (Fig. 7). Consequently, the resulting value for mass flow in the closed ports is almost negligible while it accurately matches CFD data in the open port (with some offset in Limit 2), catching both supersonic and subsonic regimes.

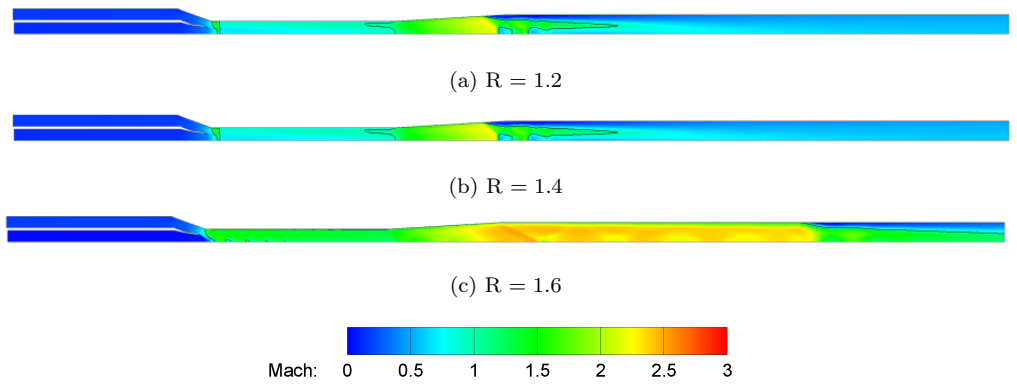
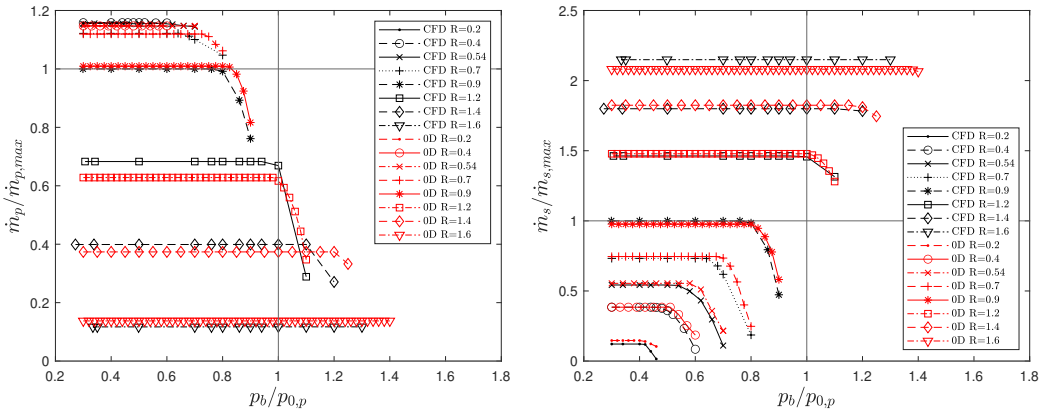


Figure 15: Mach number maps obtained from RANS simulations in Inverted Mode (Zone 1b) with R ranging from 1.2 to 1.6. Fixed $\frac{P_b}{P_p} = 0.4$.



(a) (b)

Figure 16: Ejector in Normal and Inverted Mode, (a) Primary mass flow as a function of back-pressure. (b) Secondary mass flow as a function of back-pressure.

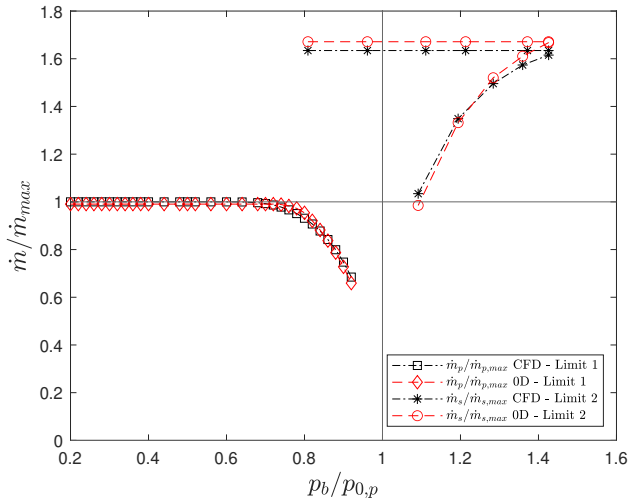


Figure 17: Mass flow rate evaluated for the cases with the secondary port (Limit 1) and primary port closed (Limit 2).

6.2. Transient operation and validation by comparison to experimental results

This validation process consists of running the 0D model by using the experimental data (pressure, temperature) as boundary conditions. Hence, mass flow signals extracted from experiments are compared to numerical

outputs. Pressure signals were analyzed and treated to obtain a suitable boundary condition for the numerical model, i.e., a filtering process was performed to obtain stable pressure signals. Mass flow signals are obtained via the vortex flow meter (VFM) in the port that is not experiencing a valve opening/closing (primary in Transition 1, secondary in Transition 2) and via a calibrated hot-wire sensor (HW) in the port that is opening/closing. The latter is necessary to detect the fast changes in the mass flow signal in real-time. The employed efficiencies are $\eta_p = 0.99$, $\eta_s = 0.9$ and $\eta_m = 0.9$.

6.2.1. Transition 1 - Closing/opening secondary

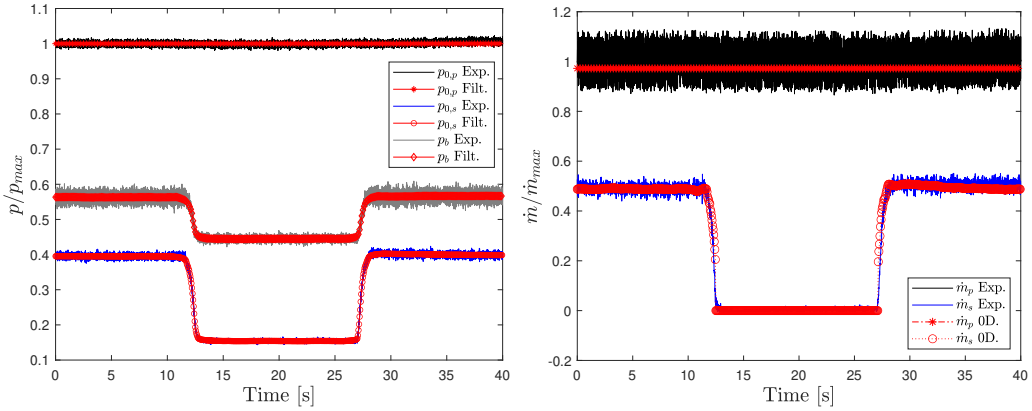
The transition is driven by the secondary valve opening/closing in 1 second. The pressures measured experimentally in the primary, secondary and back ports are shown in Fig. 18a, together with the filtered signal. As reproduced in Fig. 18b, the 0D model is capable of faithfully reproducing the experimental mass flow, both in the normal operating mode (before valve closing), during the transition, and in the case of the secondary closed port (after valve closing). Moreover, the flow characteristics are recovered after the valve is opened again. A weak fluctuation can be seen in the secondary mass flow obtained numerically just before closing and after the opening. This can be explained by the fact that the numerical secondary mass flow is determined as unchoked at the initial and final times. During the transitions, as p_{s0} starts reducing, p_b also reduces. This combined effect generates the fluctuation in the $\dot{m}_s$ curve just before the decay. The average error for the mass flow (with respect to the experimental) in the primary throughout the simulation is 2.7 %, while that on the secondary is 3.9 %. The transition is highlighted within the operational map in Fig. 20a. It shows how the ejector operates within the Normal Mode region (Zone 1a) and moves towards and backward from the secondary closed region (Limit 1). This case was already partially explained in [46], however, it is reported here to complete the information and to provide a comprehensive treatment of the relevant transition phenomena.

6.2.2. Transition 2 - Closing/opening primary

The transition is driven by the primary opening/closing in 1 second. The pressures measured experimentally in the primary, secondary and back ports are shown in Fig. 19a, together with the filtered signal. As depicted in the picture's zoom, as the primary valve is closed, the secondary pressure stabilizes at a value slightly higher than the primary, driving a secondary mass

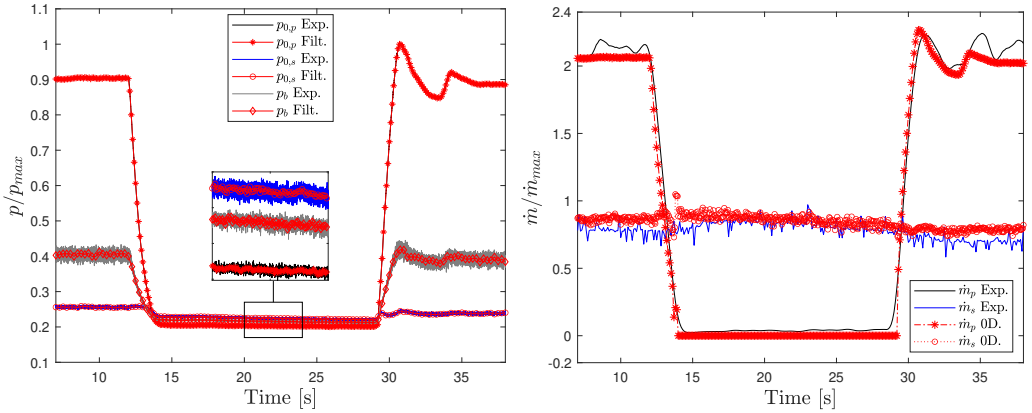
flow to the back port. Primary and secondary flow signals are characterized by a certain instability after the valve opening (at $t > 30s$), correctly captured by the filtered signals. As reproduced in Fig. 19b, the 0D model is capable of faithfully reproducing the experimental mass flow, both in the normal operating mode (before valve closing), during the transition, and in the case of the primary closed port (after valve closing). The secondary mass flow in the primary closed mode is slightly higher than in Normal Mode due to the fact that $\dot{m}_s$ is not initially choked while it reaches that condition as the valve is closed. The flow characteristics are recovered after the valve is opened again. Some discrepancy is found in primary mass flow in initial and final conditions: the 0D model provides a stable value while the experimental signal oscillates slightly. Some of those oscillations does not coincide with oscillations in the pressure signals, thus, they are not considered physically consistent. The average error for the mass flow (with respect to the experimental) in the primary throughout the simulation is 7.9 %, while that on the secondary is 8.4 %.

The transition is highlighted within the operational map in Fig. 20b. It shows how the ejector operates within the Normal Mode region (Zone 1a) and moves towards and backward from the Primary Closed region (Limit 2), passing through the Inverted zone region (Zone 1b). The passage through Zone 1b is not relevant in terms of accuracy, as it occurs only in transient operation (closing and opening of the valve). However, its correct modelization is needed to guarantee the robustness of the simulation during the transition.



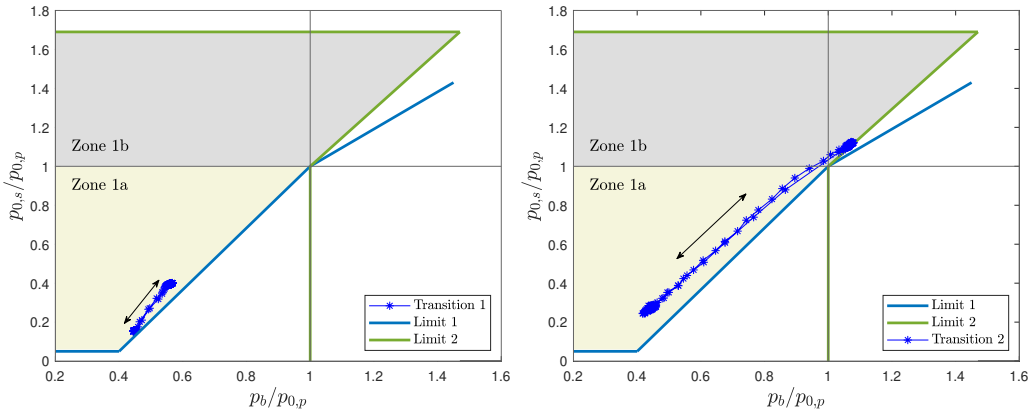
(a) Pressure signals (b) Mass flows

Figure 18: Transition 1. Pressure signals and comparison between mass flows from experimental data and 0D model.



(a) Pressure signals (b) Mass flows

Figure 19: Transition 2. Pressure signals and comparison between mass flows from experimental data and 0D model.



(a) Transition 1 (b) Transition 2

Figure 20: Transitions simulated with the 0D model placed within the ejector operational map in terms of $\frac{P_b}{P_p}$ and $\frac{P_s}{P_p}$.

7. Robustness tests on the Modelica software

In this section, the implementation of the ejector model as a Modelica object is explained and two examples of possible operation simulated by means of the simulation software are proposed, showing the flexibility and robustness of the tool. As an additional application example, the case reported in [47] shows the capability of switching from Normal Mode to a Secondary Closed mode (Transition 1) and the consequent impact of the ejector on the downstream heat exchanger inlet and outlet conditions.

7.1. Modelica object implementation

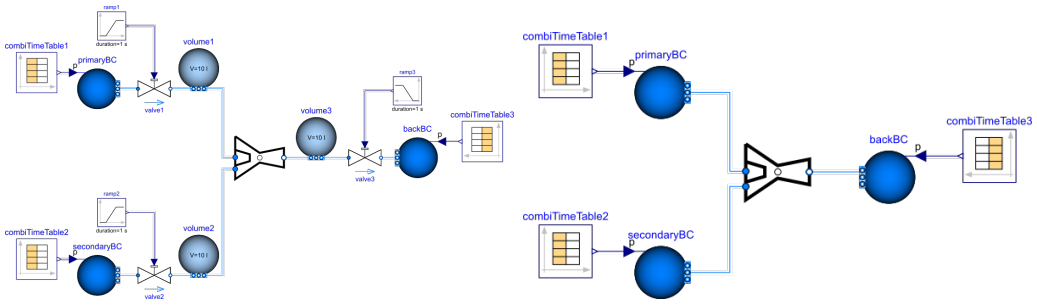
One of the main objectives of the current research is to implement the 0D ejector model as an object to be introduced within more complex thermal systems (e.g. UHBR engine bleed air system). Hence, one must focus on its robustness of implementation and execution speed, apart from delivering accurate results, as shown in Sec. 6 for dynamic analysis and in past works for static cases [16, 45, 47]. The model was developed in the Modelica/Dymola platform [50], due to its ability to handle large and complex system architectures involving multiple physics.

The 0D model employs a single physical model (introduced in Sec. 4.2) for all the operational regimes, i.e., those that can operate in steady-state regimes: Normal (Zone 1a), Inverted (Zone 1b) and Primary and Secondary

Closed Modes (Limit 1 and 2). However, to allow a robust model implementation that can cover any proper or improper operational conditions, additional formulations are needed to handle reverse flow regimes, i.e. those marked by Zones 2-6.

In general, reverse flow does not happen in operational regimes but can only occur during short transitions. Consequently, a realistic physical model that allows the accurate evaluation of reverse flow is not strictly required, and their only role is to allow robust calculation through transitions. The formulation employed in the present work to handle reverse flows is based on maintaining the consistency of mass flow vs. pressure relations using the flow resistance analogy. Mass flows are evaluated as $\dot{m}_{\mathrm{p,rev}} = (p_{p0} - p_y)K_{\mathrm{p,lim}}$, for primary flow, and as $\dot{m}_{\mathrm{s,rev}} = (p_{s0} - p_y)K_{\mathrm{s,lim}}$, for secondary flow, being p_y the pressure in the mixing section. $K_{\mathrm{p,lim}}$ and $K_{\mathrm{s,lim}}$ are numerical parameters to be tuned for each set-up. The transition between normal and reverse flow is marked by mathematical relations (usually linear) on the operational map, function of $\frac{P_b}{P_p}$ and $\frac{P_s}{P_p}$. Such relations can be obtained empirically through CFD simulations, as described in [51].

A typical Modelica set-up is depicted in Fig. 21a, where boundary conditions are set in terms of pressure at the three ports of the ejector object. Valves block the flow in ports that are to be opened/closed. A small leak is kept through closed ports to keep the consistency of the model, and volumetric sources are employed at each port to represent the piping's internal volume, which may act as an internal inertia during transitions.



(a) Complete set-up (b) Simplified set-up

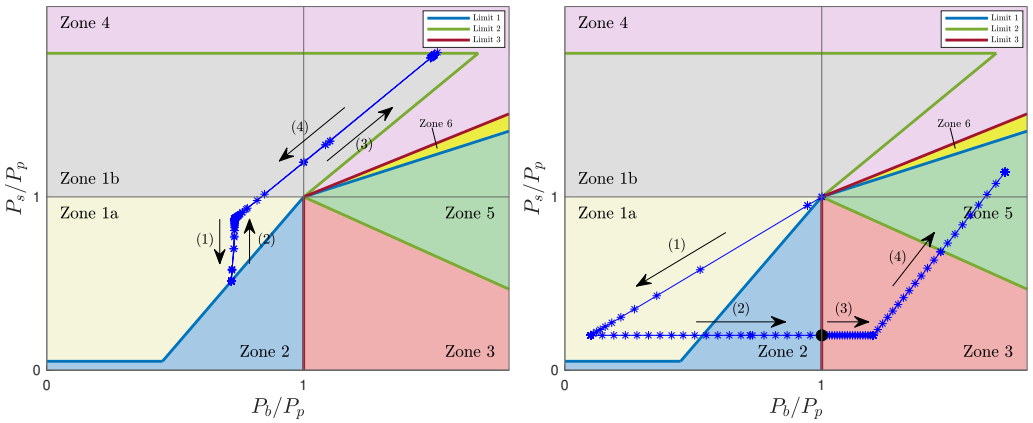
Figure 21: Modelica set-up employed for the robustness tests.

7.2. Robustness tests

Two different tests are performed in this section. In **Test A**, the two transitions treated in the present paper are reproduced sequentially, i.e., Transition 1 (closing and opening of secondary valve) and Transition 2 (closing and opening of primary valve) are executed sequentially. The simulated system is reported in Fig. 21a (linear ramps represent transitions of 1s duration), while the transition is represented in the operational map of Fig. 22a. The system is initially in Normal Mode (Zone 1a), and the flows are stable and supersonic through primary and secondary ports. Pressure and mass signals are reported in Fig. 23. After 1s, the secondary valve (valve 2) starts to close according to a linear ramp (Step (1) in the operational map plot). The transition leads the ejector to work on Limit 1, i.e., $\dot{m}_s \simeq 0$, while $\dot{m}_p$ remains stable at its maximum value, as no changes are experienced by the primary choked flow. Fig. 23a reports the pressure signals, where the pressure in the mixing zones, p_y is also represented. One can notice that, as the valve is closed, p_y equals P_s, thus naturally enhancing the zero flow through that port due to the null pressure difference. In Step (2), starting at $t = 4$ s, the valve is opened again, and the flow restores its initial state. In Step (3), starting at $t = 5$ s, the primary valve (valve 1) is closed: P_p falls and reaches p_y, leading to no flow through the primary port while $\dot{m}_s$ is unaffected. During the transition, the system passes temporarily in the Inverted Mode (Zone 1b - no stable operation in this area) to finally reach Limit 2 without robustness issues. After Step (4), triggered at $t = 8$ s, the primary valve opens again and the system restores its normal behavior.

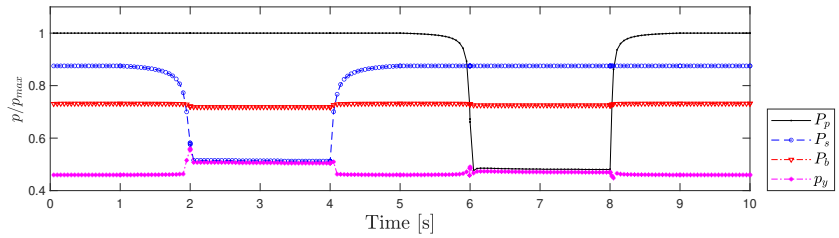
Test B consists of performing a non-realistic transition in the operational context of a flight, aimed at verifying the ability to transit through any operational mode without code robustness issues. The simulated system is reported in Fig. 21b, where no valves are employed, and boundary conditions are changed in terms of pressure signals (provided through table inputs). The aim is to avoid the dependence of a valve model when abnormal modes are occurring and analyze the stability of the ejector object alone. The transition is represented in the operational map of Fig. 22b. Please consider that, while Limit 1 was fully determined using CFD simulations, the limits between direct and reverse flows in abnormal regimes (i.e., Limit 2 and 3 for $\frac{P_s}{P_p} < 1$) are here traced according to arbitrary relations, and the flow resistances introduced in the past section are not physically relevant. Indeed, a comprehensive analysis of reverse flow operation and a consequent realistic

physical model was not a purpose of the current analysis, especially focused on the flexibility and robustness of the model. At the beginning of the simulation, the ejector is not working as both $\frac{P_s}{P_p}$ and $\frac{P_b}{P_p}$ are equal to 1. As the primary pressure rises (Step (1), from $t = 0$ s to $t = 0.5$ s), see Fig. 23a, the ejector starts working in Normal mode (Zone 1a), and mass flows rapidly reach stable values, as depicted in Fig. 23b. In Step (2), going from $t = 2$ s to $t = 3$ s, P_b rises linearly to equalize P_p. During the transition, a secondary reverse flow appears, coinciding with the passage through Zone 2, while the backflow reduces to zero. Hence, after P_b equals P_p, no flow goes through the backport, and a reverse flow is established, going from primary to secondary. The point at the end of Step (2) coincides with Limit 3. In Step (3), going from $t = 5$ s to $t = 6$ s, P_b rises further, and a reverse flow is established through the back port. However, $\dot{m}_p$ is still positive, placing the operation within Zone 3. In Step (4), going from $t = 7$ s to $t = 8$ s, P_p is reduced while P_s increases. During this transition, after crossing Limit 2 $\dot{m}_p$ becomes negative, and the final point of operation lies within Zone 5.

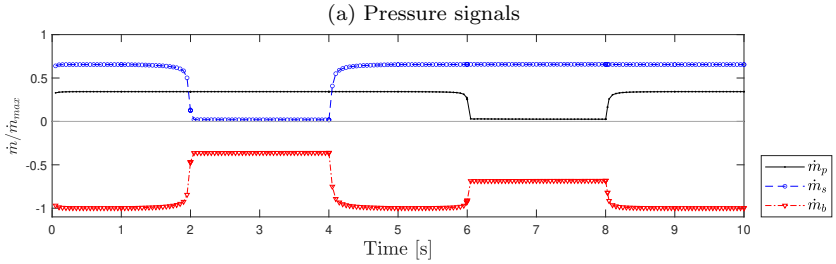


(a) Test A (b) Test B

Figure 22: Complex transitions simulated in the Modelica robustness tests.

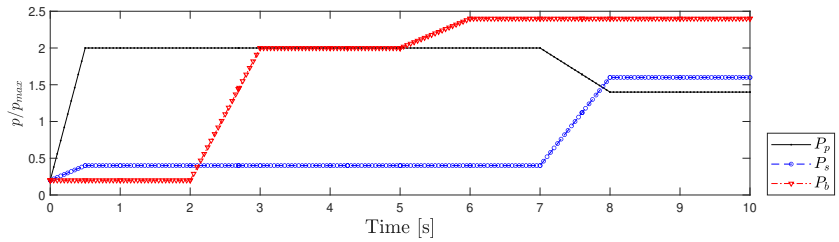


(a) Pressure signals

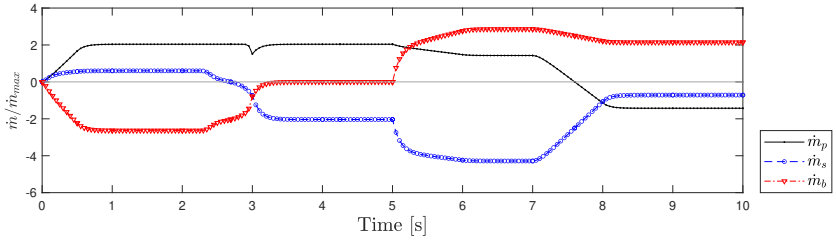


(b) Mass flows

Figure 23: Pressure signals used as boundary conditions and mass flow results obtained from the Modelica Test A.



(a)



(b)

Figure 24: Pressure signals used as boundary conditions and mass flow results obtained from the Modelica robustness test.

8. Conclusions

In this work, the transient operation of an ejector has been analyzed using an experimental set-up and numerical methods. The analysis aims to demonstrate the possibility of simulating transient scenarios representing the main transitions within the operational envelope using a novel 0D model and performing an experimental validation.

In Sec. 5.1, the quasi-static nature of the ejector was demonstrated in the operational perimeter of the system using an experimental test reproducing the dynamic closing and opening of the secondary port. The results obtained during the transient operation matched the static tests with good accuracy regarding boundary pressures and mass flows, validating the quasi-steady assumption.

Next, three different URANS tests were performed to measure the time-scale of the ejector with more precision. In the first case, Sec. 5.2.1, a sudden increment in driving pressure is set, showing that the ejector requires approximately 15 ms to adapt to the abrupt change in boundary conditions. In the second and third cases, linear time-dependent profiles of the driving pressure (or mass flow rate) between two reference pressure levels were imposed. Different time-spans were considered to replicate the transition between normal operation modes (Sec. 5.2.2) and the scenario of the primary valve closure (Sec. 5.2.3). For a transition time of 100 ms, a small offset is still observed on the primary flow rate for the whole transition, whereas, for timescales larger than or equal to 500 ms, the flow field inside the ejector can be considered quasi-steady with very good accuracy.

In Sec. 2, the operational envelope of the ejector in UHBR engine bleed systems, previously presented in [16] is summarized, highlighting the ejector regimes that should be physically modeled to allow the correct modelization of transient operation by means of 0D models. Hence, in Sec. 6.1, it is shown how the 0D model from [16] can be extended and employed to cover all the relevant operational envelope and transitions. The proposed validation covers operating points in the Inverted (Zone 1b) and Primary Closed (Limit 2) Modes, where the role of primary and secondary ports is inverted. Next, in Sec. 6, the model is validated by comparison to experimental data obtained on the two main transitions that an ejector system may experience: the opening and closure of primary and secondary ports. The agreement shows to be very good along all the represented processes. Finally, in Sec. 7, the 0D model shows its robustness when implemented in general-purpose system modeling

Modelica by allowing the simulation of unrealistic and drastic transitions through any of the operational regimes.

Acknowledgments

This project has received funding from the Clean Sky 2 Joint Undertaking (JU) under grant agreement No 101008100. The JU receives support from the European Union's Horizon 2020 research and innovation programme and the Clean Sky 2 JU members other than the Union.





Disclaimer: The contents presented in this article reflect only the author's point of view: the authors and Clean Sky JU are not responsible for any use that may be made of the information it contains.

Carles Oliet, as a Serra Húnter Associate Professor, acknowledges the Catalan Government for the support through this Program. Computational resources have been provided by the supercomputing facilities of the Université catholique de Louvain (CISM/UCL) and the Consortium des Équipements de Calcul Intensif en Fédération Wallonie Bruxelles (CÉCI) funded by the Fond de la Recherche Scientifique de Belgique (F.R.S.-FNRS) under convention 2.5020.11 and by the Walloon Region.

References

[1] G. Besagni, R. Mereu, F. Inzoli, Ejector refrigeration: A comprehensive review, Renewable and Sustainable Energy Reviews 53 (2016) 373–407.

[2] H. Yang, C. Yang, X. Zhang, X. Yuan, Influences of different architectures on the thermodynamic performance and network structure of aircraft environmental control system, Entropy 23 (7) (2021) 855.

[3] C. Vinay, C. Bhaskar, S. Malisetty, Aero-thermodynamic design of jet pump for a turboprop aircraft engine in pusher configuration, in: 5th International and 41st National Conference on Fluid Mechanics and Fluid Power (FMFP-2014), IIT Kanpur, 2014.

[4] J.-Y. Zhang, C. Wang, S. Yang, F.-N. Cheng, J.-X. Geng, Z.-X. Yang, Y.-W. Lyu, L. Yu, Research on performance of multi-nozzle ejector

for aeroengine air system, Thermal Science and Engineering Progress 38 (101651) (2023).

[5] S. He, Y. Y. Li, R. Wang, Progress of mathematical modeling on ejectors, Renewable and Sustainable Energy Reviews 13 (8) (2009) 1760–1780.

[6] B. Huang, J. Chang, C. Wang, V. Petrenko, A 1-D analysis of ejector performance, International Journal of Refrigeration 22 (5) (1999) 354–364.

[7] W. Chen, M. Liu, D. Chong, J. Yan, A. B. Little, Y. Bartosiewicz, A 1D model to predict ejector performance at critical and sub-critical operational regimes, International Journal of Refrigeration 36 (6) (2013) 1750–1761.

[8] N. S. Kumar, K. T. Ooi, One dimensional model of an ejector with special attention to Fanno flow within the mixing chamber, Applied thermal engineering 65 (1-2) (2014) 226–235.

[9] A. Metsue, R. Debroeyer, S. Poncet, Y. Bartosiewicz, An improved thermodynamic model for supersonic real-gas ejectors using the compound-choking theory, Energy 238 (2022) 121856.

[10] S. Braccio, N. Guillou, N. Le Pierrès, N. Tauveron, H. T. Phan, Mass-flowrate-maximization thermodynamic model and simulation of supersonic real-gas ejectors used in refrigeration systems, Thermal Science and Engineering Progress 37 (2023) 101615.

[11] Y. Zhou, G. Chen, X. Hao, N. Gao, O. Volovyk, A theoretical model for performance evaluation of a novel configuration of supersonic ejectors, Applied Thermal Engineering (2023) 120867.

[12] K. Wang, L. Wang, R. Gao, An extended mechanism model of gaseous ejectors, Energy 264 (2023) 126094.

[13] O. Lamberts, P. Chatelain, N. Bourgeois, Y. Bartosiewicz, The compound-choking theory as an explanation of the entrainment limitation in supersonic ejectors, Energy 158 (2018) 524–536.

[14] G. Besagni, R. Mereu, P. Chiesa, F. Inzoli, An integrated lumped parameter-CFD approach for off-design ejector performance evaluation, Energy Conversion and Management 105 (2015) 697–715.

[15] Y. Zhu, Y. Li, New theoretical model for convergent nozzle ejector in the proton exchange membrane fuel cell system, Journal of Power Sources 191 (2) (2009) 510–519.

[16] E. Schillaci, J. Vera, C. Oliet, J. B. Vemula, M. Duponcheel, Y. Bartosiewicz, Numerical modeling of air ejectors covering supersonic, subsonic and closed-port operations, Energy 302 (2024) 131627.

[17] J. Van den Berghe, B. R. Dias, Y. Bartosiewicz, M. A. Mendez, A 1D model for the unsteady gas dynamics of ejectors, Energy 267 (2023) 126551.

[18] A. Jafarian, M. Azizi, P. Forghani, Experimental and numerical investigation of transient phenomena in vacuum ejectors, Energy 102 (2016) 528–536.

[19] F. Liu, H. Liu, Y. Liu, G. Yu, X. Zhao, Y. Fan, C. Peng, Q. Li, Transient numerical study of CO2 two-phase flow in a needle adjustable ejector, International Journal of Heat and Mass Transfer 214 (2023) 124395.

[20] G. Besagni, F. Inzoli, Computational fluid-dynamics modeling of supersonic ejectors: Screening of turbulence modeling approaches, Applied Thermal Engineering 117 (2017) 122–144.

[21] G. Besagni, N. Cristiani, L. Croci, G. R. Guédon, F. Inzoli, Computational fluid-dynamics modelling of supersonic ejectors: Screening of modelling approaches, comprehensive validation and assessment of ejector component efficiencies, Applied Thermal Engineering 186 (2021) 116431.

[22] G. Grazzini, A. Milazzo, F. Mazzelli, Ejectors for efficient refrigeration: Design, applications and computational fluid dynamics, Springer, 2018.

[23] Y. Zhu, W. Cai, C. Wen, Y. Li, Numerical investigation of geometry parameters for design of high performance ejectors, Applied Thermal Engineering 29 (5-6) (2009) 898–905.

[24] J. Gagan, K. Smierciew, D. Butrymowicz, J. Karwacki, Comparative study of turbulence models in application to gas ejectors, International Journal of Thermal Sciences 78 (2014) 9–15.

[25] Y. Zhu, P. Jiang, Experimental and numerical investigation of the effect of shock wave characteristics on the ejector performance, International journal of refrigeration 40 (2014) 31–42.

[26] A. Hemidi, F. Henry, S. Leclaire, J.-M. Seynhaeve, Y. Bartosiewicz, CFD analysis of a supersonic air ejector. Part I: Experimental validation of single-phase and two-phase operation, Applied Thermal Engineering 29 (8-9) (2009) 1523–1531.

[27] Y. Bartosiewicz, Z. Aidoun, P. Desevaux, Y. Mercadier, Numerical and experimental investigations on supersonic ejectors, International Journal of Heat and Fluid Flow 26 (1) (2005) 56–70.

[28] S. Croquer, S. Poncet, Z. Aidoun, Turbulence modeling of a single-phase R134a supersonic ejector. Part 2: Local flow structure and exergy analysis, International Journal of Refrigeration 61 (2016) 153–165.

[29] T. Sriveerakul, S. Aphornratana, K. Chunnanond, Performance prediction of steam ejector using computational fluid dynamics: Part 2. flow structure of a steam ejector influenced by operating pressures and geometries, International Journal of Thermal Sciences 46 (8) (2007) 823–833.

[30] O. Lamberts, P. Chatelain, Y. Bartosiewicz, Numerical and experimental evidence of the Fabri-choking in a supersonic ejector, International Journal of Heat and Fluid Flow 69 (2018) 194–209.

[31] B. H. Park, J. H. Lim, W. Yoon, Fluid dynamics in starting and terminating transients of zero-secondary flow ejector, International Journal of Heat and Fluid Flow 29 (1) (2008) 327–339.

[32] V. Lijo, H. D. Kim, G. Rajesh, T. Setoguchi, Numerical simulation of transient flows in a vacuum ejector-diffuser system, Proceedings of the Institution of Mechanical Engineers, Part G: Journal of Aerospace Engineering 224 (7) (2010) 777–786.

[33] R. Arun Kumar, G. Rajesh, Effect of geometric configurations on the starting transients in vacuum ejector, AIAA Journal 57 (7) (2019) 2905–2922.

[34] G. Bharate, G. Arun Kumar, Starting transients in second throat vacuum ejectors for high altitude testing facilities, Aerospace Science and Technology 113 (2021) 106687.

[35] S. Afkhami, N. Fouladi, M. P. Fard, Experimental and numerical investigation of transient starting of pre-evacuated exhaust diffuser in high altitude ground test, Aerospace Science and Technology 133 (2023) 108111.

[36] N. Fouladi, S. Afkhami, M. Pasandideh F., Starting transient analysis of second throat exhaust diffuser in high-altitude test of a thrust optimized parabolic nozzle, Physics of Fluids 35 (6) (2023).

[37] S. Afkhami, N. Fouladi, Gas dynamics at starting and terminating phase of a supersonic exhaust diffuser with a conical nozzle, Physics of Fluids 36 (3) (2024).

[38] Z. Liu, Z. Liu, K. Jiao, Z. Yang, X. Zhou, Q. Du, Numerical investigation of ejector transient characteristics for a 130-kW PEMFC system, International Journal of Energy Research 44 (5) (2020) 3697–3710.

[39] J. Han, B. Zhao, Z. Pang, J. Feng, X. Peng, Transient characteristics investigation of the integrated ejector-driven hydrogen recirculation by multi-component cfd simulation, International Journal of Hydrogen Energy 47 (67) (2022) 29053–29068.

[40] X. Wang, J. Zheng, Z. Hao, Y. Di, X. Miao, Study on the effect of pulsed gas flow on the entrainment performance of hydrogen ejector, International Journal of Hydrogen Energy 67 (2024) 599–607.

[41] S. Croquer, O. Lamberts, S. Poncet, S. Moreau, Y. Bartosiewicz, Large Eddy Simulation of a supersonic air ejector, Applied Thermal Engineering 209 (2022) 118177.

[42] B. H. Park, J. H. Lim, W. Yoon, Fluid dynamics in starting and terminating transients of zero-secondary flow ejector, International Journal of Heat and Fluid Flow 29 (1) (2008) 327–339.

[43] M. H. Eldakamawy, M. V. Sorin, M. Brouillette, Blowdown experimental study on butene ejector, Applied Thermal Engineering 160 (2019) 114000.

[44] M. Raju, S. Desikan, A. Vaidyanathan, Transient characteristics of a typical vacuum ejector—an experimental study, Physics of Fluids 34 (9) (2022).

[45] E. Schillaci, C. Oliet Casasayas, J. B. Vemula, M. Duponcheel, Y. Bartosiewicz, P. Planquart, Air ejector analysis in normal and abnormal modes, oriented to control purposes in aircraft systems, in: 9th European Conference for Aeronautics and Space Sciences (EUCASS), European Conference for AeroSpace Sciences (EUCASS), 2022, pp. 1–12.

[46] E. Schillaci, C. Oliet Casasayas, J. B. Vemula, M. Duponcheel, Y. Bartosiewicz, P. Planquart, Air ejector analysis in extended operational perimeter for control oriented simulation of bleed-air aircraft systems, in: Journal of Physics: Conference Series, Vol. 2526, IOP Publishing, 2023, p. 012057.

[47] E. Schillaci, C. Oliet Casasayas, N. Ablanque Mejía, S. Torras Ortiz, J. B. Vemula, M. Duponcheel, Y. Bartosiewicz, P. Planquart, A 0D approach for extended operational modeling of air ejectors in thermal systems, in: International Heat Transfer Conference 17: August, 14-18, 2023, Cape Town, South Africa: proceedings, Begell House, 2023.

[48] J. Van den Berghe, M. Delsipee, P. Planquart, Y. Bartosiewicz, M. A. Mendez, Calibration of a 1D ejector model from full-scale experiments, ASTFE Digital Library 8 (2023) 1151.

[49] F. Mazzelli, A. B. Little, S. Garimella, Y. Bartosiewicz, Computational and experimental analysis of supersonic air ejector: Turbulence modeling and assessment of 3D effects, International Journal of Heat and Fluid Flow 56 (2015) 305–316.

[50] S. E. Mattsson, H. Elmqvist, M. Otter, Physical system modeling with modelica, Control engineering practice 6 (4) (1998) 501–510.

[51] E. Schillaci, J. B. Vemula, M. Duponcheel, Calibration of the 0D model of an air ejector by means of compressible RANS simulations, in: ICHMT DIGITAL LIBRARY ONLINE, Begel House Inc., 2023.